Development of a tendon driven robotic probe for prostate palpation. *

Francis Chikweto, *Student Member ,IEEE,* Takeshi Okuyama, *Member, IEEE*, and Mami Tanaka

Abstract— **Palpation is a clinical diagnosis method utilized by physicians to acquire valuable information about the pathological condition of an organ using the sense of touch. This method, however, is subjective. The accuracy depends on the physician's experience and skill. Therefore, to make palpation objective and minimize variability in prostate cancer diagnosis among physicians, an automated palpation system is required. This paper describes the design and experimental evaluation of a 2 Degrees of Freedom (2DoF) tendon driven robotic palpation probe. The probe's palpation motion is controlled by actuating driving tendons using a cable-differential pulley transmission system and a return spring. A kinematic model of the robotic probe was derived. Furthermore, a tendon path length model was geometrically determined, and an optimization method for guide arc center placement to minimize change in tendon length was presented. Preliminary experimental and theoretical results were compared to determine the positioning accuracy. The difference between theoretical pitch angles $[0^{o},80^{o}]$ and measured values for the yaw angle range of $[0^{o}, 40^{o}]$ was found to be in the range of $0.03^{o} \sim 5.06^{o}$.**

Clinical Relevance— **Diagnosis based on manual palpation is often subjective and palpation sensitivity depends on the physician's level of experience and skill . Therefore, an objective method for acquiring tactile information is relevant. Robotic palpation system provides objective and quantitative information for better understanding of the pathological and physiological changes in the tissue using mechanical properties as biomarkers.**

I. INTRODUCTION

Prostate cancer is the second most commonly occurring cancer in men and the fourth most commonly occurring cancer overall [1]. As a standard clinical procedure for prostate cancer screening, physicians commonly use a digital rectal examination (DRE), and serum prostate specific antigen (PSA) blood test [2,3]. DRE is readily available, cost effective, and possess lower risk. DRE combined with PSA blood test, could enhance early detection rate of prostate cancers [4]. However, DRE results are subjective and lack objective and quantitative information. The effectiveness depends highly on the examiner's level of experience [5,6]. Furthermore, evidence from some studies suggests that DRE may not significantly reduce mortality, but instead may result in a high number of false positives leading to unnecessary invasive diagnostic tests that can result in pain, erectile dysfunction, and overdiagnosis [7-9].

Tremendous progress has been made towards the development of various prostate tissue assessment methods and devices based on direct characterization of mechanical properties of the prostate and imaging such as Ultrasound (US), Magnetic Resonance Imaging (MRI) and elastography [10,11]. Recently, robotic technology has successfully been adopted in the medical field with many surgical robotic systems such as Da Vinci systems commercially on the market and in active research [12,13]. Success attributed to commercial surgical robots has propelled the development of robotic devices for the detection of tumors. Various robotic palpation systems, and tactile sensor systems for the evaluation of tissue mechanical properties have been developed. Results from laboratory-based experiments have demonstrated good success, although currently they have not been adopted for clinical practice and most of them are only based on ex vivo experimental setup [14,15]. Ahn *et al.* have worked on a robotic palpation system to map mechanical properties of the prostate and improve prostate cancer detection [16]. Tanaka *et al.* developed an active palpation system which was used for clinical in vivo tests on human prostates to distinguish tumors from normal tissue [17].

Image guided biopsy (Transrectal Ultrasound and MRI) serves as the gold standard for diagnosis confirmation of prostate cancer when a suspected case is identified during DRE. Despite having poor sensitivity and subject to significant inter-and intra-observer variability, DRE is still predominantly used for prostate cancer screening. Thus, improving upon the inaccuracies associated with this prostate cancer screening modality by leveraging robotics and tactile sensors is eminent. This research aims at developing an in vivo robotic palpation system for direct mechanical assessment of the prostate. This paper specifically focuses on the kinematic performance evaluation of the probe.
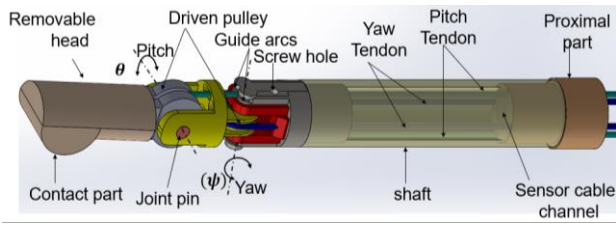
II. ROBOTIC PALPATION PROBE DESIGN

A. Palpation Probe Structure

A conceptual design of the robotic palpation probe and prototype are shown in Fig. 1. A hollow shaft connects the proximal and distal end of the probe. The main structure is a simple 2DoF wrist consisting of yaw and pitch revolute joints with their axes of rotation perpendicular to each other. Joint motions are mechanically decoupled from each other for easy controllability.

T. Okuyama is with the Department of Robotics, Graduate School of Engineering, Tohoku University, Aoba-ku, Sendai,Japan:Phone:022-795-5879; fax: 022-759-5897; e-mail: takeshi.okuyama.e7@tohoku.ac.jp).

F .Chikweto is with the Department of Biomedical Engineering, Graduate School of Biomedical Engineering, Tohoku University, Aoba-ku, Sendai, Japan. (e-mail: chikweo.francis.q3@dc.tohoku.ac.jp).

M. Tanaka is with the Department of Biomedical Engineering, Graduate School of Biomedical Engineering, Tohoku University, Aoba-ku, Sendai, Japan (e-mail: mami.tanaka.e6@tohoku.ac.jp).

(a) Conceptual design

(b) Palpation probe prototype

Figure 1. Robotic palpation probe

Two steel tendons (SUS304,diameter 0.45 mm) are used to actuate the joints. They pass through the articulation wrist via four wire guide holes of 1.2 mm in diameter, located 10 mm radially away from the center of the wrist and wrap around the driven pulley of each joint. One end of each driving tendon is fixed to a sliding pulley of a differential drive actuator and the other end to a return spring. Guide arcs are placed on the yaw part of the wrist to prevent acute bending of the pitch tendon on the sharp or small round edges when the probe yaws, which leads to reduced durability of the tendon. Non-movable guide arcs lead to a simpler construction of the tool wrist and reduce the number of moving components. A similar design concept of guide arcs has been used in the wrist mechanism for robot assisted laparoscopic surgery [18].Furthermore, attached to the distal end of the probe is a disposable probe head which serves as a contact material between the probe and the prostate.

For future consideration of sensor placement on the distal end, the probe has a channel for routing tactile or contact force sensor cables from the distal to the proximal part of the probe. Currently in this prototype, a different approach for contact force sensing is adopted.

The developed tendon-driven palpation probe is designed to mimic finger motions of physicians during manual palpation procedures for tumor detection and in surgery. The outer diameter of the probe is reduced to minimize discomfort and injury. The target dimensions of this prototype are 14 mm maximum outer diameter and 135 mm length. Besides the wires and joint bearings, all the main parts of the probe are 3D printed from Polylactic acid (PLA) material.

The concept for robotic palpation procedure is as follows; A probe is inserted into the rectum of the patient and manipulated using tendons driven by an actuator system placed outside the patient. By controlled palpation, the contact part of the probe applies pressure on the prostate similar to that applied by the physician's finger. In this prototype, contact force is estimated by measuring tensions of the driving tendons using load cells positioned outside the patient, between the proximal part of the probe and the actuator system due to size

constraints of the commercially available force sensors. Estimated contact force and indentation depth information is then used to estimate stiffness of the prostate tissue.

B. Robot Kinematic Modelling

Forward kinematics: Forward kinematics problem for the probe's revolute joints is resolved using the Denavit-Hartenberg (D-H) method. Coordinate frames based on D-H convention for each segment are shown in Fig. 2. Obtained D-H parameters are specified in TABLE I, where $l_1 = 15 \ mm$, $l_2 = 22 \ mm$, $i = 1,2$. Joint variables ψ and θ range between $\pm 90°$.

From the D-H parameters in TABLE I, the homogenous transformation matrix is formulated as

$$H_2^0 = \begin{bmatrix} cs\psi cs\theta & -cs\psi s\theta & s\psi & cs\psi(l_2 cs\theta + l_1) \\ s\psi cs\theta & -s\psi s\theta & -cs\psi & s\psi(l_2 cs\theta + l_1) \\ s\theta & cs\theta & 0 & l_2 s\theta \\ 0 & 0 & 0 & 1 \end{bmatrix}, \quad (1)$$

where $cs\psi = cos\psi$, $s\psi = sin\psi$, $cs\theta = cos\theta$, $s\theta = sin\theta$. Consequently, the position $P = [x \ y \ z]^T$ relative to the base frame O is derived as,

$$P = \begin{bmatrix} x \\ y \\ z \end{bmatrix} = \begin{bmatrix} cs\psi(l_2 cs\theta + l_1) \\ s\psi(l_2 cs\theta + l_1) \\ l_2 s\theta \end{bmatrix}. \quad (2)$$

Kinematic mapping: Transformation between various spaces of the kinematic model for the palpation probe is shown in Fig. 3. The user input represents the desired palpation angles $q_d = [\psi_d \ \theta_d]^T \in [-90°, 90°]$ commanded by the user. Commanded angles are then mapped to corresponding motor rotations $\omega = [\omega_y \ \omega_p]^T$. Given the desired palpation angles, the desired target position $P_d = [x_d \ y_d \ z_d]^T$ can be determined using (2). The actuator space consists of two tendon–pulley transmission systems to drive each joint independently. Each driving mechanism comprises two 3D printed concentric differential input pulleys of radii r_1^{in} and r_2^{in} mounted on a servo motor shaft. Radius r_1^{in} is slightly larger than r_2^{in}.
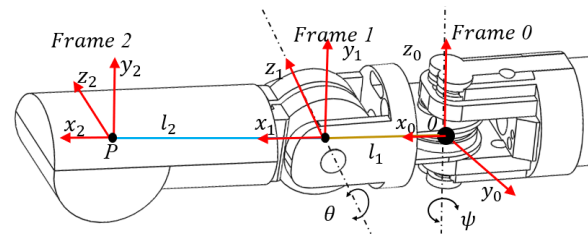

Figure 2. Probe coordinate frames

TABLE I. D-H parameters

Axis	Link length $r_{i-1}(mm)$	Twist angle $\alpha_{i-1}(Deg)$	Link offset $d_i(mm)$	Joint Variable (Deg)
1	l_1	$90°$	0	ψ
2	l_2	0	0	θ

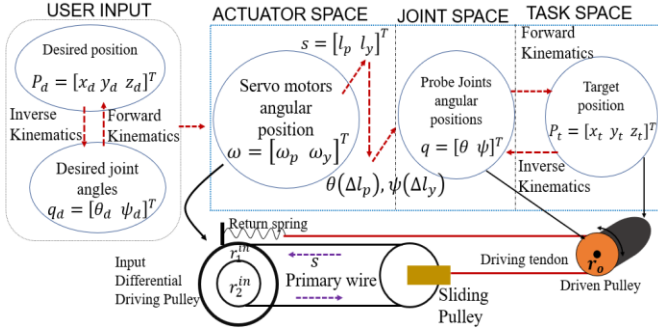Figure 3. Kinematic mapping

A sliding pulley is connected to the input differential pulleys by a primary wire s and to the driven pulley of radius r_o by a driving tendon. A return spring is used as a passive actuator. When the input pulleys and servo motor turn clockwise and counterclockwise by ω, a primary wire s unwinds and winds from the input pulleys, translating the sliding pulley forward and backwards, respectively. Provided there is no slack in the actuator space, motor rotation ω results into shortening or elongation of each primary wire Δs given by,

$$\Delta s = \left(\frac{r_1^{in} - r_2^{in}}{2}\right)\begin{bmatrix}\omega_p \\ \omega_y\end{bmatrix}. \tag{3}$$

Driven pulleys for the two joints actuated by each respective driving tendon rotate by $q = [\theta \ \psi]^T$. A mapping of yaw and pitch motor rotations $\boldsymbol{\omega} = \begin{bmatrix}\omega_y & \omega_p\end{bmatrix}^T$ to joint angles q is given by,

$$\boldsymbol{\omega} = \left(\frac{2r_o}{r_1^{in} - r_2^{in}}\right)q = Dq = D\begin{bmatrix}\theta \\ \psi\end{bmatrix}, \tag{4}$$

where D is the reduction ratio. From (4), a very high and potentially infinite reduction ratio can be obtained simply by adjusting the size of the input pulley radii.

Tendon length model: Fig. 4 shows the path of the pitch tendon at three distinct yaw ψ angle positions. The offset distance l_1 between the yaw and pitch centers of rotation is given in the D-H parameter TABLE I. During yaw motion, if no guide arc or pulley is present, the length of the pitch tendon is constant about any angle ψ. However, sharp, and small round edges would wear the tendon fast and increase friction as the probe pivots about the yaw axis. Guide arcs are therefore, used to provide a minimum turning radius required for transmission, increasing tendon durability of the tendon, and reduction in permanent stretch of the tendon over multiple uses, which may cause backlash and affect the positioning accuracy. Circular guide arcs 1 and 2 are mirrored to each other about the shaft's plane of symmetry.

Consider guide arc 1 when the probe rotates about the yaw axis by ψ and moves from the initial position to position 1. For a given yaw angle ψ, the coordinates $B(x_b, y_b)$ with respect to the yaw origin $O(0,0)$ can be expressed as

$$x_b = l_1 \cos(\psi) \ , \ y_b = l_1 \sin(\psi). \tag{5}$$
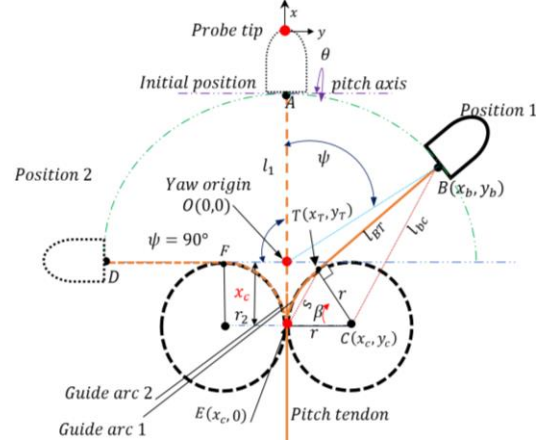

Figure 4. Tendon length model

The distance l_{bc} between the guide arc center $C(x_c, y_c)$ and point $B(x_b, y_b)$ is expressed as

$$l_{bc} = \sqrt{(x_b - x_c)^2 + (y_b - y_c)^2} . \tag{6}$$

Tangent segment l_{BT} can be obtained by

$$l_{BT} = \sqrt{l_{bc}^2 - r^2} \quad , \tag{7}$$

where r is the radius of the guide arc. The contact point $T(x_T, y_T)$ between the segment l_{BT} and the circular guide arc is found by (8).

$$\begin{bmatrix}x_T \\ y_T\end{bmatrix} = \begin{bmatrix}x_c + \frac{(x_b - x_c)r^2 + r(y_c - y_b)\sqrt{(x_b - x_c)^2 + (y_b - y_c)^2 - r^2}}{(x_b - x_c)^2 + (y_b - y_c)^2} \\ y_c + \frac{(y_b - y_c)r^2 + r(x_b - x_c)\sqrt{(x_b - x_c)^2 + (y_b - y_c)^2 - r^2}}{(x_b - x_c)^2 + (y_b - y_c)^2}\end{bmatrix}. \tag{8}$$

Using the calculated contact points and the length of the chord S connecting point T and E, the angle β subtended by the arc length l_{TE} can be calculated using the law of cosines.

$$\beta = arccos\left(1 - \frac{S^2}{2r^2}\right) = arccos\left(1 - \frac{(x_T - x_c)^2 + y_T^2}{2r^2}\right) \tag{9}$$

The arc length l_{TE} can be calculated by $l_{TE} = \beta r$. The common tangent l_{BT} between T and B is given by

$$l_{BT} = \sqrt{(x_b - x_T)^2 + (y_b - y_T)^2} . \tag{10}$$

Therefore, the entire length of the tendon segment l_{BE} can be calculated as

$$l_{BE} = l_{BT} + l_{TE} . \tag{11}$$

The initial length l_{AE} of the tendon segment at $\psi = 0°$ is expressed as

$$l_{AE} = l_1 + x_c. \tag{12}$$

In the ideal state, the tendon path length must remain the constant for all $\psi \in [0, 90°]$. In other words, $l_{AE} = l_{BE}$. Hence, the change in tendon length $\varepsilon(x_c, \psi, l_1, r) = l_{AE} - l_{BE}$ becomes the objective function for minimization. Optimization is achieved by finding the optimum $(x_c{}^*)$ values in the $[-r, 0]$ search space for which this objective function is minimum.

$$(x_c{}^*) = \frac{argmin(\varepsilon(x_c, \psi, l_1, r))}{x_c \in [-r, 0]} \qquad (13)$$

Optimization of the guide arc center: In this section, an optimization procedure for placement of guide arcs is explained. At the initial position when $\psi = 0°$, guide arc center is positioned such that $x_c = r$ below the yaw O origin. To avoid bending the tendon at the arc-shaped guide end, the guide arc is always set tangentially to the x-axis such that $y_c = r$. The length of the pitch tendon remains constant.

$$l_{AE} = l_1 + r \qquad (14)$$

In position 2 the tendon path is of length l_{DE} when ψ is 90°. The pitch tendon curves along the arc-shaped guide of radius $r_2 = r$.

$$l_{DE} = l_1 + \frac{\pi r}{2} - r \qquad (15)$$

The change in tendon length between the two positions can be calculated by $\varepsilon = l_{AE} - l_{DE} = \left(2 - \frac{\pi}{2}\right)r \approx 0.4292r$. To minimize the previous tendon length error, optimization can be done by shifting x_c upwards by $\left(2 - \frac{\pi}{2}\right)r$, towards the yaw origin O such that the center is $x_c = \left(\frac{\pi}{2} - 1\right)r \approx 0.5708r$. Under this condition the cable length remains approximately constant for ψ -90, 0 and +90° angles.

For any range of motion $\psi\epsilon[-90°, 90°]$, optimization method for finding guide arcs which route the tendon around the yaw joint while minimizing the stretch can be achieved. Tendon stretch can be minimized by adjusting the center C, as follows; Start with $(90°, x_c = -r)$ as initial conditions as shown above. Find the lengths of the tendon segment using (11) for $\psi\epsilon[-90°, 90°]$. Find the change in length and perform optimization using (13). Translate x_c upwards by a distance equal to the change in length for this range of motion. This results into a new center, and the new reduced stretch in the tendon. Repeat shifting position x_c towards the yaw origin until a minimum change in tendon length ε is found.

III. EXPERIMENTAL SETUP

Fig. 5 shows a schematic diagram of the experimental setup for measuring positioning accuracy of the point P coordinates of interest. The cable pulley actuator system consisted of two concentric differential pulleys of radius 4 and 5 mm, mounted on a servo motor (Parallax Feedback 360° High Speed Servo) and a sliding pulley. Return springs served as passive actuators. A proportional-derivative (PD) control algorithm was embedded on a Micro Controller Unit (MCU) Arduino Mega for motor angle control via a PC. Position measurement of the point P was achieved by tracking infrared reflection markers installed on the probe using an optical 3D
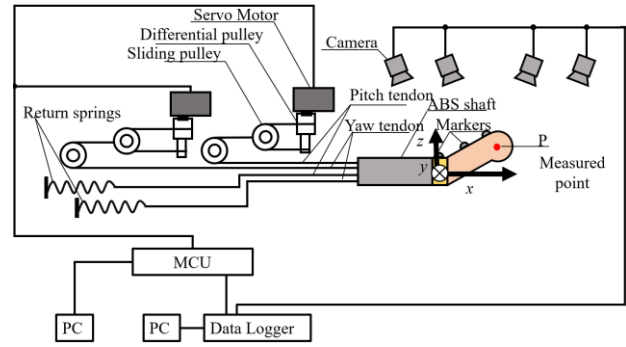

Figure 5. Experimental setup for measuring position *P*.

motion capture system (Inter Reha, VICON) with four infrared cameras (Inter Reha, MX-T160, 16 million pixels).The sampling rate for the motion capture system was set at 100 Hz.

Experimental conditions were set for ψ and θ variables according to the predefined 6 paths. The yaw angle ψ was varied between $[0°, 50°]$ in increments of 10°. For each defined ψ, the probe was rotated about the pitch θ between $[0°, 80°]$ in the similar 10° increment. The offset length l_1 between the yaw and the pitch axis was set to 15 mm. The distance l_2 between the pitch axis and the measured point P was 22 mm.

IV. RESULTS

In this section, simulation results for optimized guide arc centers essential for tendon length change minimization and positioning accuracy based on (2) are presented, respectively.

Fig. 6 shows change in tendon length in the vicinity of optimized guide arc center positions. The guide arc radius was 1.5 mm. Results in Fig. 6 show that the tendon length change ε is maximum in the $\psi\epsilon[54°, 61°]$ region. Furthermore, the negative sign signifies that the tendon length decreases. Since the tendon is pre-tensioned to prevent backlash, the length becomes shorter.

Fig. 7 shows root mean square (RMS) of the tendon length change for $\frac{l_1}{r} = 10$ and $\frac{l_1}{r} = 20$. It is evident that the ratio of the length of the offset link l_1 between the pitch and yaw axis to the guide arc radius r has effect on the RMS of the tendon length change.
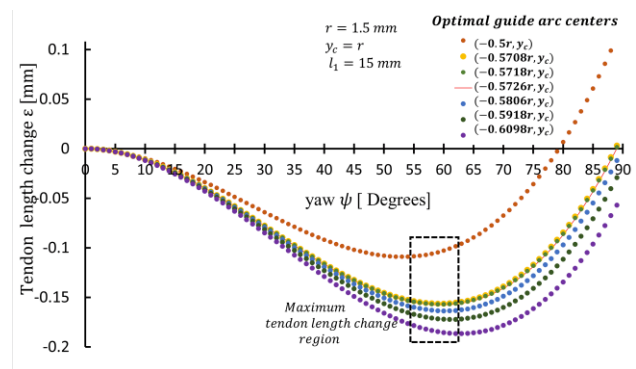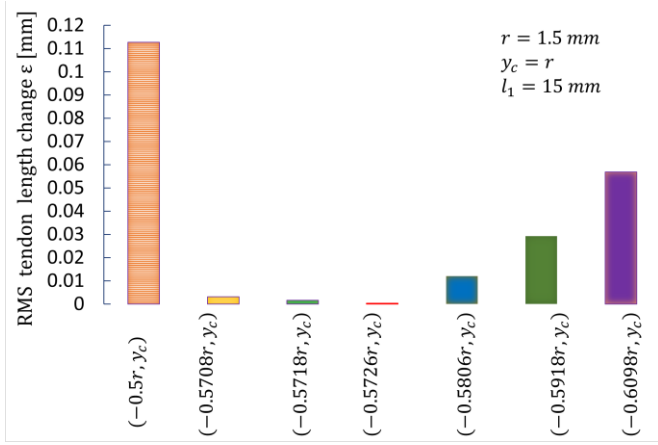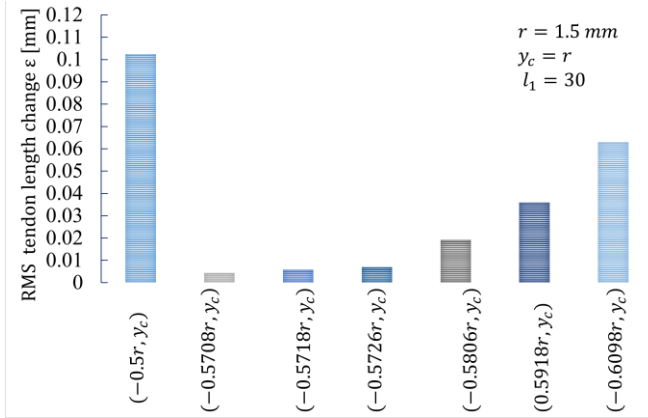

Figure 6. Theoretical change in tendon length in the vicinity of guide arc optimized center positions.

(a) $\frac{l_1}{r} = 10$

(b) $\frac{l_1}{r} = 20$

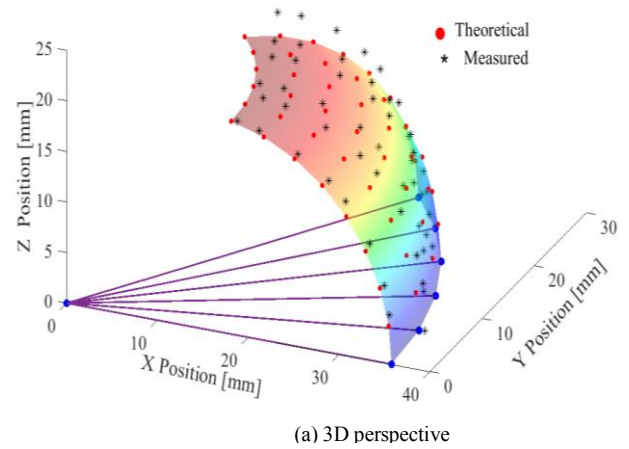Figure 7. Root-mean-square (RMS) values for tendon length change

(a) 3D perspective

(b) Top view

Figure 8. Theoretical and measured P position.

Desired parameters such as the guide arc radius r ,offset length l_1 and guide arc center can, therefore, be decided based on the model with the smallest RMS value. In this paper, $\frac{l_1}{r} = 10$ ratio and guide center $C(-0.5726r, r)$ were the preferred parameters for the robotic probe owning to their yielded smallest RMS value.

A comparison between experimental results for P position and theoretical values obtained from (2) is shown in. Fig. 8. Results show a notable difference between the measured and theoretical trajectory at yaw $\psi = 50°$ (path 6) compared to other paths when $\psi \in [0°, 40°]$.
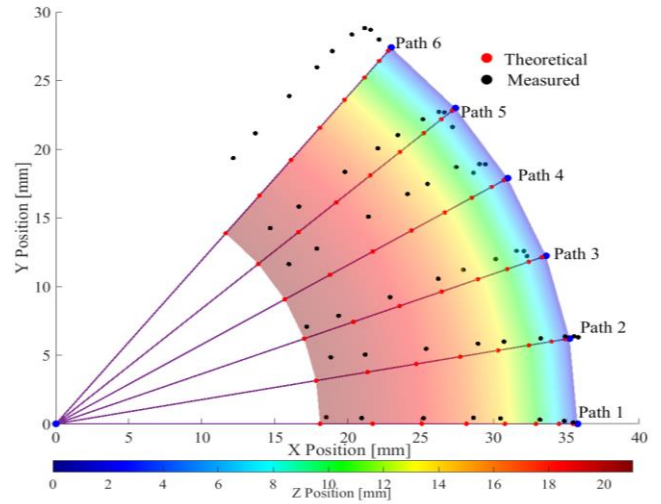
Likewise, theoretical pitch angles for $\psi \in [0°, 40°]$ were compared with the reconstructed pitch angles from measured position data in TABLE II. A comparison between the measured pitch angles $[0°, 80°]$ and theoretical values under $\psi \in [0°, 40°]$ condition revealed an error angle ranging between $0.03° \sim 5.06°$.

V. DISCUSSION AND CONCLUSION

In this study, a tendon driven robotic palpation probe was fabricated and its kinematic performance evaluated. Optimum guide arc centers to minimize stretch of the pitch tendon as the probe pivots about the yaw axis were determined.

TABLE II. Comparison of measured pitch angles

Set Yaw ψ		0°	10°	20°	30°	40°
Theoretical Pitch angles θ	0	0.032	0.14	0.60	1.91	0.13
	10	12.96	12.09	10.80	10.28	9.82
	20	20.59	19.90	17.42	16.38	15.10
	30	31.88	31.56	29.26	27.13	25.89
	40	44.76	44.15	41.86	39.81	37.65
	50	51.28	50.34	49.64	46.70	44.94
	60	61.72	61.13	61.64	58.63	56.82
	70	71.49	70.69	72.50	72.46	70.34
	80	77.52	74.95	78.46	79.10	78.57

The accuracy of the probe's motion was experimentally determined using a motion capture system. Specifically, experimental values of the point P position were compared with theoretical values. The positioning accuracy of the current prototype for $\psi \in [0°, 40°]$ showed promising results with pitch angle error ranging between $0.03° \sim 5.06°$. However, at $\psi = 50°$ there was relatively a large deviation

in the y position and vertically the probe was unable to reach in the reasonable vicinity maximum pitch angle of $80°$.

The possible causes of positioning error are friction in the system, mechanical cross talk between joints, and slight bending of the 3D printed input differential pulleys during pulling since the primary cable is under high tension. From these results, it is suggested that the accuracy can be improved by further optimizing the guide arc center so as to minimize tendon length change in the $\psi\epsilon[50°, 61°]$ vicinity, replacing the plastic 3D printed PLA input differential pulleys with metallic ones, and reducing pulley-cable friction by using other smoother cable materials as a substitute for steel tendons. Simulation results from the tendon length model showed that the optimal offset x_c for minimum RMS is sensitive to the ratio of the yaw-pitch axis offset distance to the arc guide radius. Therefore, this ratio and its corresponding RMS value can be used in the design process to determine the optimal preferred model. The system presented in this paper is the first prototype and several design iterations are required in order to improve on the performance limitations highlighted. The results obtained so far make it suitable for further research consideration. Neither human subjects nor animals were included in any experimental procedures in this study, hence getting approval was trivial.

The future scope of this work will focus on the improvement of positioning accuracy, contact force estimation using measured tension in the driving tendons, mechanical properties characterization of prostate phantoms, and miniaturization of the actuator system. Several tests will need to be carried out using the complete palpation system before conducting in vivo clinical trials as follows; experimentation on tissue phantoms followed by ex vivo tests on porcine samples with embedded hard nodules to represent possible tumors and then on excised human prostate samples upon obtaining approval.

REFERENCES

[1] IARC, 2019. International Agency for Research on Cancer. [Online] Available at: http://gco.iarc.fr/today/home[Accessed 16 February 2021].

[2] J. Ramon, and L. J. Denis, "Prostate Cancer: Recent Results in Cancer Research," Springer: Berlin/Heidelberg/New York, 2007.

[3] A.W. Partin, et al., "Analysis of percent free prostate-specific antigen (PSA) for prostate cancer detection: influence of total PSA, prostate volume, and age," *Urology*, 1996, vol.48, pp.55–61.

[4] M. J. Gosselaar, et al., "Screening for Prostate Cancer at Low PSA Range: The Impact of Digital Rectal Examination on Tumor Incidence and Tumor Characteristics," *The Prostate*, 2006, vol. 67, pp. 154-161.

[5] D.S. Smith and W.J. Catalona, "Interexaminer variability of digital rectal examination in detecting prostate cancer," *Urology*, 1995, vol.45, pp. 70-74.

[6] T. Okuyama, S. Yokoyama, Y. Tanahashi, and M. Tanaka, "Measurement of palpation motion using prostate examination simulator and motion capture system," *Mech. Eng. J.*, vol. 3, no. 1, 2016, doi: 10.1299/mej.15-00539.

[7] L. Naji, et al., "Digital rectal examination for prostate cancer screening in primary care: a systematic review and meta-analysis," *The Annals of Family Medicine*, 2018, vol.16, no.2, pp.149-154.

[8] T. Cui, R. C. Kovell, R, P. Terlecki, "Is it time to abandon the digital rectal examination? Lessons from the PLCO Cancer Screening Trial and peer-reviewed literature," *Curr Med Res Opin.*, 2016, vol.32, no.10, pp.1663-1669.

[9] K. Jugita, P. Landis, B. K. Mcneil, and C. P. Pavlovich, "Serial prostate biopsies are associated with an increased risk of erectile dysfunction in men with prostate cancer on active surveillance," *J Urol* ; 2009, vol.182, pp.2664–2669.

[10] D. W. Good, et al., "Elasticity as a biomarker for prostate cancer: a systematic review," *BJU Int.*, 2014, vol.113, pp. 523–534.

[11] N. P. Kelly, et al., "Direct mechanical characterization of prostate tissue - a systematic review," *Prostate*, 2019, vol.79, pp.115– 125.

[12] H. M. Le, T. N. Do, and S. J. Phee, "A survey on actuators-driven surgical robots," *Sens. Actuators Phys.*, 2016, vol. 247, pp.323–354.

[13] F. Jelínek, et al., "Classification of Joints Used in Steerable Instruments for Minimally Invasive Surgery - A Review of the State of the Art," *J. Med. Devices*, 2015, vol. 9, no. 1, doi: 10.1115/1.4028649.

[14] M. Li, et al., "Intra-operative tumour localisation in robot-assisted minimally invasive surgery: A review" *Proceedings of the Institution of Mechanical Engineers, Part H: Journal of Engineering in Medicine*, 2014, vol.228, no.5, pp.509-522.

[15] W. C. Carson, et al., "Material characterization of ex vivo prostate tissue via spherical indentation in the clinic," *Med Eng Phys*, 2011, vol.33, pp.302–309.

[16] B. Ahn, et al., "Robotic palpation-based mechanical property mapping for diagnosis of prostate cancer," *J Endourol*, 2011, vol.25, pp.851–857.

[17] M. Tanaka, M. Furubayashi, Y. Tanahashi, and S. Chonan, "Development of a palpation sensor for detection of prostate cancer and hypertrophy", *Smart Mater Struct.*, 2000, vol.9, pp.878–884.

[18] M. Jinno, "Simple noninterference mechanism between the pitch and yaw axes for a wrist mechanism to be employed in robot-assisted laparoscopic surgery," *ROBOMECH J.*, 2019, vol.6, no.1, doi: 10.1186/s40648-019-0129-y.